PNAS RESEARCH ARTICLE | IMMUNOLOGY AND INFLAMMATION

Structural insights into KSHV-GPCR constitutive activation and CXCL1 chemokine recognition

Aijun Liu[a,b,1], Yezhou Liu[a,1], Clàudia Llinàs del Torrent Masachs[c,1], Weijia Zhang[a], Leonardo Pardo[c,2], and Richard D. Ye[a,d,2]

Affiliations are included on p. 10.

Edited by Robert Lefkowitz, HHMI, Durham, NC; received February 15, 2024; accepted August 21, 2024

Kaposi's sarcoma-associated herpesvirus (KSHV) encodes a viral G protein-coupled receptor, KSHV-GPCR, that contributes to KSHV immune evasion and pathogenesis of Kaposi's sarcoma. KSHV-GPCR shares a high similarity with CXC chemokine receptors CXCR2 and can be activated by selected chemokine ligands. Like other herpesvirus-encoded GPCRs, KSHV-GPCR is characterized by its constitutive activity by coupling to various G proteins. We investigated the structural basis of ligand-dependent and constitutive activation of KSHV-GPCR, obtaining high-resolution cryo-EM structures of KSHV-GPCR–Gi complexes with and without the bound CXCL1 chemokine. Analysis of the apo-KSHV-GPCR–Gi structure (2.81 Å) unraveled the involvement of extracellular loop 2 in constitutive activation of the receptor. In comparison, the CXCL1-bound KSHV-GPCR–Gi structure (3.01 Å) showed a two-site binding mode and provided detailed information of CXCL1 binding to a chemokine receptor. The dual activation mechanism employed by KSHV-GPCR represents an evolutionary adaptation for immune evasion and contributes to the pathogenesis of Kaposi's sarcoma. Together with results from functional assays that confirmed the structural models, these findings may help to develop therapeutic strategies for KSHV infection.

Kaposi's sarcoma | chemokine | KSHV-GPCR | CXCL1 | cryo-EM structure

Significance

KSHV-GPCR is a cell surface receptor encoded by the genome of Kaposi's sarcoma-associated herpesvirus that, when expressed in host cells, causes angiogenic tumor of proliferative endothelial cells. The present study investigates the structural basis for constitutive activation of KSHV-GPCR and its modulation by chemokines. Our structural models indicate that KSHV-GPCR uses its extracellular loop 2 for self-activation without ligand stimulation, but it retains the ability of binding and responding to the chemokine CXCL1 that further enhances its angiogenic activity. Our findings demonstrate structural features for the unique dual activation mechanism employed by this viral GPCR for immune evasion and angiogenic proliferation, that may be targeted for antiviral therapy.

Kaposi's sarcoma-associated herpesvirus (KSHV), also termed human herpesvirus-8 (HHV8), is a γ2-herpesvirus and the etiologic agent of Kaposi's sarcoma (KS), a multifocal spindle-cell tumor (1, 2). In addition to KS, the virus causes primary effusion lymphoma, multicentric Castleman's disease, and KSHV inflammatory cytokine syndrome (3). As a double-stranded DNA virus, KSHV has a genome of around 165,000 base pairs that encode many homologs of mammalian proteins, likely pirated by the virus from its mammalian host cells (4). These hijacked genes code for functional orthologs of interleukin-6, Bcl-2, cyclin-D, the chemokines CCL2 and CCL3, interferon regulatory factors, and a G protein-coupled receptor (GPCR) in KSHV (5, 6). Altogether, these genes are believed to contribute to KSHV viral immune evasion and the pathogenesis of KS.

Among the virus-encoded proteins of KSHV, KSHV-GPCR (encoded by *ORF74*) contributes to immune responses, tumor transformation, and angiogenesis (7, 8). KSHV-GPCR is highly expressed by the host cell during the lytic cycle (2), which is characterized by the upregulation of KSHV-GPCR and other lytic proteins including viral interferon regulatory proteins that inhibit type I interferons. In addition, the expression of host genes, particularly cytokines interleukin 6 and CXCL1, are up-regulated by coexpression of KSHV-GPCR with cell-type specificity (9). The expression of KSHV-GPCR also elicits VEGF-mediated angiogenesis in a paracrine manner (10, 11). It has been suggested that the oncogenic mechanism of KSHV highlights KSHV-GPCR, which can activate NF-κB and AP-1 signaling pathways and induce the expression of growth factors, cytokines, and chemokines (12, 13). *In vivo* studies also suggest that transgenic expressing KSHV-GPCR could cause Kaposi's sarcoma-like tumors (14). These findings point out the ability of KSHV to modulate host responses for immune evasion (15, 16).

KSHV-GPCR shares a high sequence similarity with human CXC chemokine receptors, especially CXCR1 and CXCR2 that bind common chemokine ligands including CXCL1, CXCL2, and CXCL8 (6). Besides, KSHV-GPCR also has ligand-independent constitutive activity (7). As a result, KSHV-GPCR may influence cellular functions similar to other chemokine receptors but without binding endogenous ligands. Several other viral GPCRs also share this striking feature of constitutive activity, including Epstein-Barr virus (EBV)-encoded BILF1, human cytomegalovirus (HCMV)-encoded US28, UL33, human herpesvirus 6 and human herpesvirus 7 (HHV6/HHV7)-encoded U12 and U51 (5, 6). The constitutive activity of viral GPCRs modulates host gene expression, cell-signaling events, and host immunity, further contributing to the survival and proliferation of the

Author contributions: A.L., Y.L., and R.D.Y. designed research; A.L., Y.L., C.L.d.T.M., W.Z., and L.P. performed research; A.L., Y.L., C.L.d.T.M., L.P., and R.D.Y. analyzed data; L.P. and R.D.Y. supervised research; and A.L., Y.L., and R.D.Y. wrote the paper.

The authors declare no competing interest.

This article is a PNAS Direct Submission.

[1]A.L., Y.L., and C.L.d.T.M. contributed equally to this work.

[2]To whom correspondence may be addressed. Email: Leonardo.pardo@uab.cat or richardye@cuhk.edu.cn.

This article contains supporting information online at https://www.pnas.org/lookup/suppl/doi:10.1073/pnas.2403217121/-/DCSupplemental.

Published October 8, 2024.

virus (15). Previous studies have investigated the downstream oncogenic signaling pathways constitutively activated by KSHV-GPCR (12, 13, 17); however, the molecular and structural basis of the ligand-independent activation of this particular viral GPCR has yet to be unraveled. Recently, a study identified the structure of BILF1 in complex with human heterotrimeric Gi protein, providing a structural basis for ligand-independent BILF1–Gi signaling (18). Previous studies have also identified structures of an apo-US27–Gi protein complex and a US28-CX3CL1–Gi protein complex (19). However, the signaling pathway downstream of US27 is still uncharacterized despite forming a constitutively inactive conformation in complex with Gi proteins. Moreover, neither US27 nor BILF1 has identified endogenous ligand, whereas KSHV-GPCR binds the ELR-positive CXC chemokines CXCL1 and CXCL2 (20). These chemokines further activate KSHV-GPCR above its constitutive levels, making KSHV-GPCR a structural and functional homolog of CXCR1 and CXCR2 with ligand-dependent and -independent activation capability (20). Here, we present the cryo-EM structure of KSHV-GPCR–Gi protein complex at an overall resolution of 2.81 Å, and the cryo-EM structure of monomeric CXCL1-bound KSHV-GPCR–Gi protein complex at an overall resolution of 3.01 Å. Functional analysis confirmed that extracellular loop 2 (ECL2) works together with conserved structural motifs for constitutive activation of KSHV-GPCR. With a nearly complete N terminal sequence of KSHV-GPCR solved (5 amino acids to the first Met), the cryo-EM structure of the CXCL1-bound KSHV-GPCR–Gi complex provides insight into the interaction of a chemokine receptor with CXCL1, which was not previously available.

Results

Overall Structures of KSHV-GPCR–Gi Complex Without and with Bound CXCL1. Stable complexes of KSHV-GPCR–Gi protein were reconstituted by coexpression of KSHV-GPCR and heterotrimeric Gi proteins in *Sf9* insect cells (*SI Appendix*, Fig. S1*A*). The purified receptor–Gi protein complexes were then subjected to single-particle cryo-EM analysis, yielding a structural model of the KSHV-GPCR–Gi complex at a global resolution of 2.81 Å (Fig. 1 *A* and *B* and *SI Appendix*, Fig. S1 *B–F*). The monomeric CXCL1-bound KSHV-GPCR–Gi complex was reconstituted by coexpression of human CXCL1 together with the receptor and Gi proteins in Sf9 cells. Single-particle analysis of the CXCL1-KSHV-GPCR–Gi complex produced a structural model at a global resolution of 3.01 Å (Fig. 1 *C* and *D* and *SI Appendix*, Figs. S2 *B–F* and S3). The reconstituted 3D structures revealed a typical seven-transmembrane (7-TM) topology of GPCRs with either ligand-free (Fig. 1*B*) or CXCL1-bound (Fig. 1*D*) TM pocket. The structures of CXCL1-bound and constitutively active KSHV-GPCR are nearly identical, with a root mean square distance (RMSD) of 0.32 Å between their Cα atoms. However, small differences are observed adjacent to the chemokine binding sites (Fig. 1 *E* and *F*). To accommodate the binding of CXCL1, ECL2 of KSHV-GPCR tilts upward, thereby disengaging the interactions with the binding cavity. TM3 bends toward the center of the transmembrane binding pocket (Fig. 1*E*). From an extracellular view of the receptor, it is well observed that the β-hairpin region of ECL2 and ECL1 move closer to the chemokine for accommodation of the chemokine core (Fig. 1*F*). In both structures, the disulfide bond between ECL1 ($C118^{ECL1}$) and ECL2 ($C196^{ECL2}$) is clearly visible, whereas the predicted disulfide bond between N terminus ($C39^{NT}$) and ECL3 ($C286^{ECL3}$) is not [Ballesteros-Weinstein numbering in superscript denotation indicates the relative position of the amino acid residue in class A GPCR, (21)]. A close examination found that the two cysteines were 3.6 Å apart, making it difficult to form a disulfide bond. The N terminal Pro-Cys (PC motif) found in most chemokine receptors becomes Val-Cys in KSHV-GPCR and lacks the bent conformation. The constitutively active KSHV-GPCR interacts extensively with the α5 helix of Gαi, and to a close proximity with the αN helix of Gαi and Gβ subunit, thereby securing the conformation of an active receptor–Gi protein complex as is commonly seen in agonist-bound Class A GPCRs (22). To verify the ligand-independent constitutive activity of KSHV-GPCR, we further examined Gi signaling of the receptor by analyzing basal levels of cAMP accumulation and G protein dissociation without ligand. In both assays, cAMP inhibition and G protein dissociation were correlated positively with the amount of input plasmid DNA coding for KSHV-GPCR (Fig. 1 *G* and *H*).

Extracellular Loop 2 Is Crucial for the Constitutive Activation of KSHV-GPCR. Constitutively active GPCRs display high basal activity without agonist binding. Previous reports illustrated the possibility that a large extracellular loop 2 (ECL2) may provide additional contacts for constitutive activation of a viral chemokine receptor (18). The ECL2 in KSHV-GPCR (a.a. 183 to 207) is the largest among the 3 extracellular loops (Fig. 2 *A* and *B*), and its role in constitutive activation of the receptor was examined by substitution of the loop with ECL2 counterparts from several other Class A GPCRs including CXCR2, FPR1, CXCR4, and CMKLR1 (Fig. 2 *C–F*). These mutants were further subjected to functional analysis using a NanoBiT-based complementation assay (23) for measurement of G protein dissociation. Basal levels of G protein dissociation were compared among different mutants and with the wild-type KSHV-GPCR control. Significantly elevated chemiluminescence signals were observed for ECL2 substituted mutants, indicating that constitutive activation of G protein was abrogated in the ECL2 substituents. These findings further suggested an important role of ECL2 in the constitutive activation of KSHV-GPCR.

To investigate how ECL2 engages in the constitutive activation of KSHV-GPCR, we focused on polar contacts between ECL2 and the rest of the receptor. Among the amino acid residues examined in the constitutively active KSHV-GPCR model, $E198^{ECL2}$ forms multiple polar bonds with $R278^{6.62}$(Fig. 2*H*). Alanine substitution of $R278^{6.62}$ was performed, and subjected to a NanoBiT-based G protein dissociation assay. As shown in Fig. 2*I*, a significantly elevated chemiluminescence signal was observed, demonstrating reduced G protein activation. The mutant was readily expressed on the cell surface (*SI Appendix*, Fig. S4). Altogether, these results imply a direct engagement of ECL2 in constitutive activation of KSHV-GPCR.

Recognition of CXCL1 by KSHV-GPCR. Next, we examined the cryo-EM structure of the CXCL1-bound KSHV-GPCR–Gi complex. CXCL1 (also termed GRO1 oncogene, GROα, and melanoma growth stimulating activity) is an agonist of KSHV-GPCR that further activates the receptor above constitutive level (20). In the CXCL1-KSHV-GPCR–Gi complex, CXCL1 was solved from A1 to I61 following the first turn of the C-terminal helix, after which there was insufficient map quality for modeling (Fig. 3*A*). As an ELR-positive chemokine, E6-L7-R8 presents an ELR motif in CXCL1. The CXC motif (C9-Q10-C11) in the N-loop forms two disulfide bonds for connections to the 30s-loop and the β3-strand (Fig. 3*A*). The globular core of CXCL1 is defined by the β1-strand, 30s-loop, β2-strand, 40s-loop, β3-strand, and a C-terminal helix. In the CXCL1-KSHV-GPCR structure, the chemokine and the receptor are in 1:1 stoichiometry, and their interaction appears to follow the two-site model (24, 25)

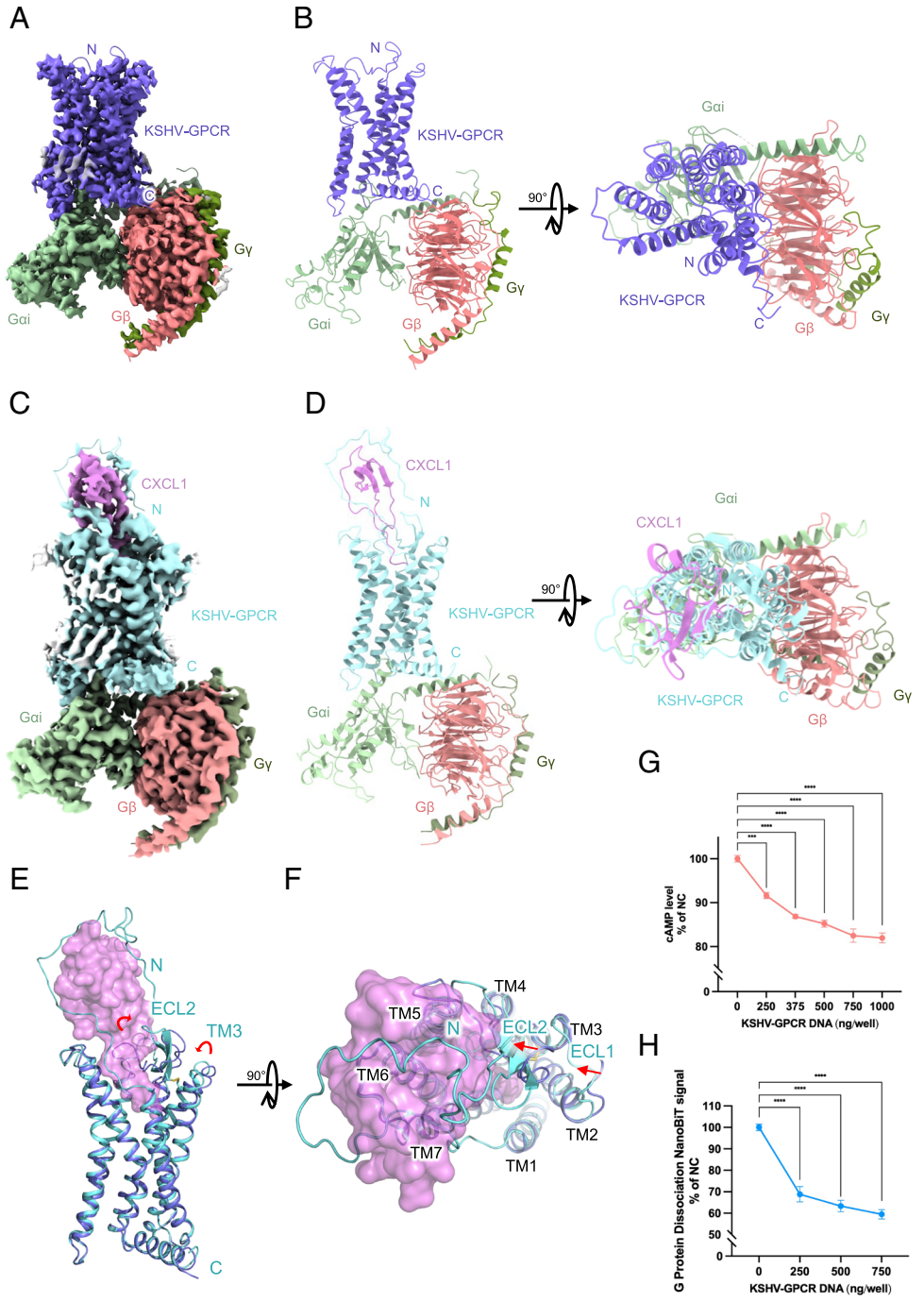

Fig. 1. Overall structure of KSHV-GPCR–Gi complex and KSHV-GPCR-CXCL1–Gi complex. (*A*) Cryo-EM map of constitutively active KSHV-GPCR in complex with heterotrimeric Gi proteins at an overall resolution of 2.81 Å. Ligand-free constitutively active KSHV-GPCR is shown in purple, Gαi in lime green, Gβ in salmon red, and Gγ in dark green. (*B*) Atomic coordinates of constitutively active KSHV-GPCR in complex with heterotrimeric Gi proteins from side view (*Left* panel) and top view (*Right* panel). Ligand-free constitutively active KSHV-GPCR is shown in purple, Gαi in lime green, Gβ in salmon red, and Gγ in dark green. (*C*) Cryo-EM map of CXCL1-bound KSHV-GPCR in complex with heterotrimeric Gi proteins at an overall resolution of 3.01 Å. CXCL1-bound KSHV-GPCR is shown in cyan, CXCL1 in magenta, Gαi in lime green, Gβ in salmon red, and Gγ in dark green. (*D*) Atomic coordinates of CXCL1-bound KSHV-GPCR in complex with heterotrimeric Gi proteins from side view (*Left* panel) and top view (*Right* panel). CXCL1-bound KSHV-GPCR is shown in cyan, CXCL1 in magenta, Gαi in lime green, Gβ in salmon red, and Gγ in dark green. (*E*) Side view of superimposed structures of CXCL1-bound KSHV-GPCR (cyan) and constitutively inactive KSHV-GPCR (purple). (*F*) Top view of superimposed structures of CXCL1-bound KSHV-GPCR (cyan) and constitutively active KSHV-GPCR (purple). An inward movement of receptor ECL1, ECL2, and TM3 was observed for CXCL1-bound KSHV-GPCR. (*G*) Basal levels of cAMP accumulation without ligand treatment. Data were shown as % of negative control (0 ng KSHV-GPCR plasmid DNA/well) and obtained from three independent experiments, each with three replicates. ***$P < 0.001$; ****$P < 0.0001$. (*H*) Basal levels of NanoBiT-based G protein dissociation without ligand treatment. Data were shown as % of negative control (0 ng KSHV-GPCR plasmid DNA/well) and obtained from three independent experiments, each with three replicates. ***$P < 0.001$; ****$P < 0.0001$.

with clearly identifiable chemokine recognition sites 1, 2, and 1.5 (CRS1, CRS2, and CRS1.5) (Fig. 3*B*). At CRS1, the globular core of CXCL1 interacts with the N terminus of KSHV-GPCR, which was solved to the 5th amino acid. Notably, the N terminus of KSHV-GPCR fits into a groove on CXCL1 in between the β1-strand and the C-terminal helix (Fig. 3*C*). Extensive hydrophobic contacts between the residue pairs are observed at CRS1, including $D5^{NT}$-S30, $F6^{NT}$-V28, $L7^{NT}$-V28, $T8^{NT}$-N27,

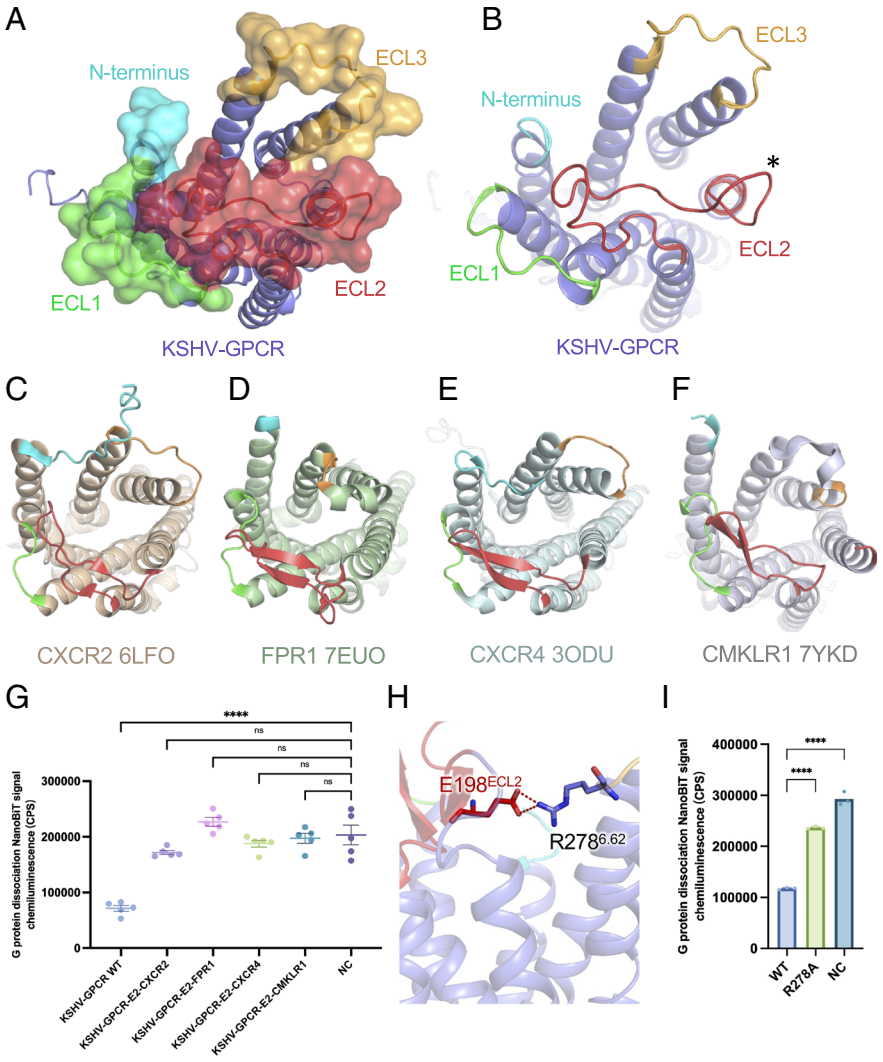

Fig. 2. Extracellular loop 2 of KSHV-GPCR is crucial for constitutive G protein activation. (*A*) The structure of constitutively active KSHV-GPCR in an extracellular view. Receptor N terminus and extracellular loops are shown as surface. N terminus loop is colored in cyan, ECL1 is marked with green, ECL2 is shown in red and ECL3 is highlighted in yellow. (*B*) The structure of constitutively active KSHV-GPCR in an extracellular view. Receptor N terminus and extracellular loops are shown as cartoon. ECL2 of KSHV-GPCR occupies a relatively large space over the canonical binding pocket of the receptor. The asterisk indicates a small region where the EM density is relatively weak due to its lack of interactions and its intrinsic flexibility. (*C*–*F*) Extracellular view of the structures of (*C*) CXCR2 (active, PDB ID: 6LFO), (*D*) FPR1 (active, PDB ID: 7EUO), (*E*) CXCR4 (inactive, PDB ID: 3ODU), and (*F*) CMKLR1 (active, PDB ID: 7YKD). (*G*) ECL2 of KSHV-GPCR was substituted by ECL2 of CXCR2, FPR1, CXCR4, and CMKLR1, respectively. Basel levels of G protein dissociation were tested and compared between mutants and wildtype control. (*H*) Polar interaction between ECL2 of KSHV-GPCR and the canonical transmembrane binding pocket. (*I*) Reduced ligand-independent constitutive G protein activation in the R278A mutant. Data were obtained from three independent experiments, each with three replicates. ****$P < 0.0001$.

I9^{NT}-V26, L11^{NT}-I23, W17^{NT}-K21 (Fig. 3*C*). In addition, multiple polar interactions are present between D13^{NT} of the receptor and K21 of CXCL1, and between Y26^{NT} of the receptor and CXCL1 K61 (Fig. 3*D*). These interactions allow the N terminus of KSHV-GPCR to wrap around the chemokine core tightly.

At CRS1.5, defined by the PC motif of chemokine receptors, extensive polar interactions hold together the receptor PC motif (VC in KSFV-GPCR) and the CXC motif of CXCL1. S37^{NT} forms two polar bonds with L12 and Q13 of CXCL1, C39^{NT} interacts with the backbone oxygen atom of Q10, and E40^{NT} interacts with K49 on the β3-strand of CXCL1 (Fig. 3*E*).

The N terminus of CXCL1 protrudes deep into the transmembrane binding pocket of the receptor that forms CRS2. Here, R289$^{7.28}$ interacts with the backbone of C9. There are two polar contacts: D274$^{6.58}$ and N293$^{7.32}$ form polar interactions with R8 of CXCL1, R212$^{5.39}$ interacts with E6, and R183$^{4.64}$ at the bottom of the binding pocket forms polar interaction with S2 of CXCL1 (Fig. 3*F*). This ELR motif at the chemokine's N terminus contributes to the main intermolecular polar interactions at CRS2. For nonpolar interactions, A1 of CXCL1 forms multiple hydrophobic contacts with L54$^{1.38}$, E103$^{2.60}$, and E121$^{3.27}$. A4 has nonpolar interactions with A297$^{7.36}$. T5 forms nonpolar interactions with Y197^{ECL2}. Moreover, the N terminus of CXCL1 favors the minor subpocket of KSHV-GPCR in proximity to TM1-3.

Functional validation of receptor–chemokine interactions was further conducted through site-directed mutagenesis and NanoBiT-based G protein dissociation assay. Alanine substitution at CRS1 (D13^{NT}A and Y26^{NT}A) did not completely eliminate G protein activation with a response of about 35% of WT remaining (Fig. 3*G*). At CRS1.5, alanine substitutions including S37A, C39A, and E40A reduced G protein activation upon CXCL1 stimulation, with a maximum response around 40% of WT and an EC_{50} comparable with WT (~1.3 × 10^{-8} M) for the S37A mutant, and a loss of both potency and efficacy for mutants C39A and E40A (Fig. 3*H*). Deep into the TM pocket, alanine substitution at CRS2 (R183A, R212A, D274A, R289A, and N293A) abrogated G protein dissociation, with a maximum response around 20% of WT and an EC_{50} comparable with WT for

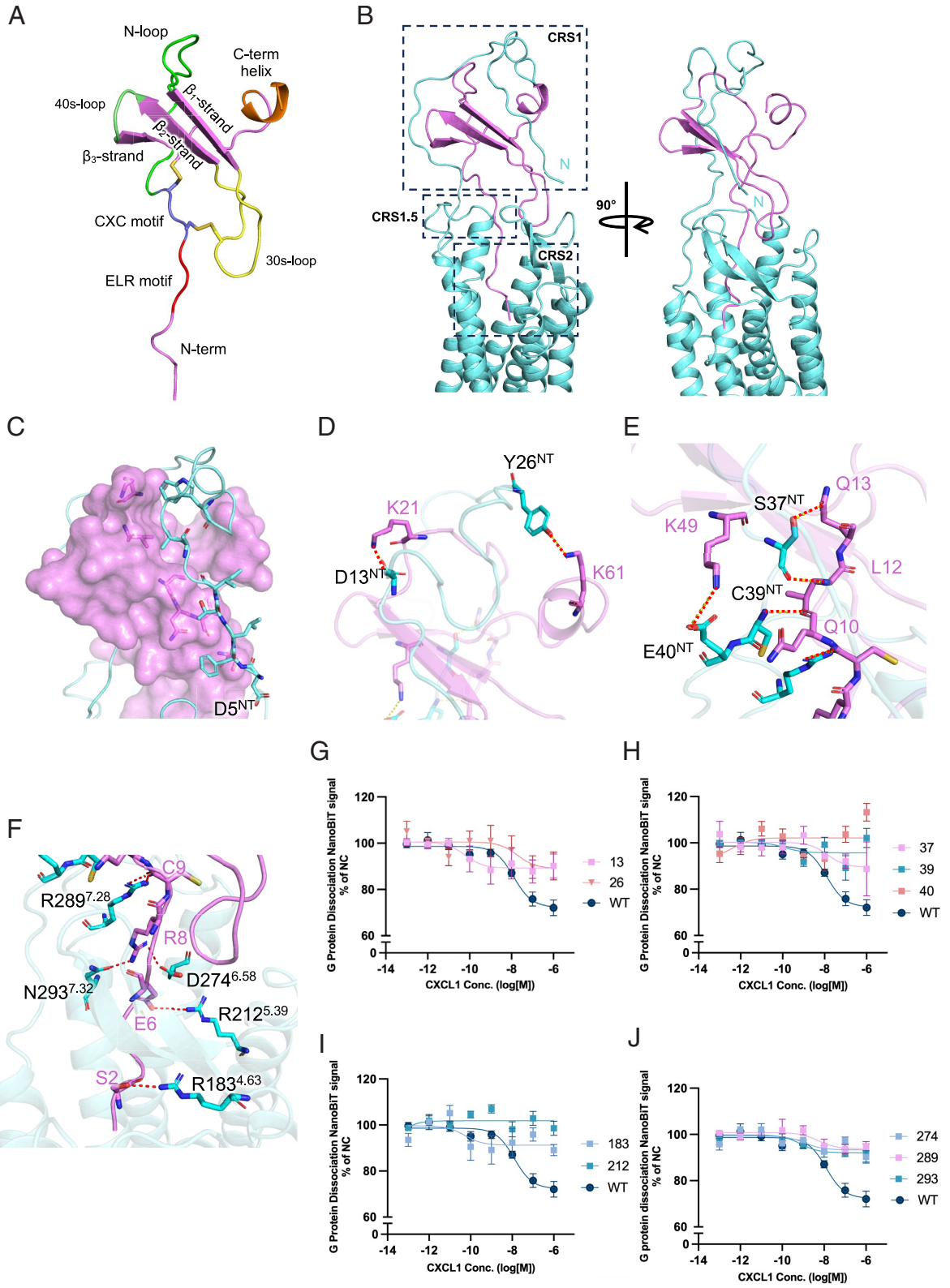

Fig. 3. Molecular interactions between CXCL1 and KSHV-GPCR. (*A*) Structure of CXCL1. Structural regions of CXCL1 are highlighted, including N terminus (magenta), ELR motif (red), CXC motif (slate blue), N-loop(green), 30s-loop (yellow), 40s-loop (grass green), β1-β3 strands (magenta), and C-terminal helix (orange). (*B*) Overview of the interaction between CXCL1 (magenta) and KSHV-GPCR (cyan). Chemokine binding sites CRS1, CRS1.5, and CRS2 are marked with dashed boxes. (*C*) The N terminus of KSHV-GPCR (resolved to the fifth amino acid D5) wraps around the globular core of CXCL1. Residues with hydrophobic interactions are shown in sticks. CXCL1 is shown in surface representation. (*D*) Polar contacts between CXCL1 and KSHV-GPCR at chemokine recognition site 1 (CRS1). Hydrogen bonds (red dashed lines) are observed between $D13^{NT}$ and K21, $Y26^{NT}$, and K61 (shown in sticks), respectively. (*E*) Polar interactions between CXCL1 and KSHV-GPCR at chemokine recognition site 1.5 (CRS1.5). (*F*) Polar interactions between CXCL1 and KSHV-GPCR at chemokine recognition site 2 (CRS2). Hydrogen bonds are highlighted in dotted lines. (*G*) NanoBiT-based G protein dissociation of CRS1 alanine substitution mutants. (*H*) NanoBiT-based G protein dissociation of CRS1.5 mutants. (*I* and *J*) NanoBiT-based G protein dissociation of alanine-substituted mutants at CRS2 residues. Data were obtained from three independent experiments, each with three replicates, and presented as percentages of the negative control without ligand treatment.

mutants D274A, R289A, and N293A and a loss of both potency and efficacy for R183A and R212A (Fig. 3 *I* and *J*). Cell surface expression of the mutants was comparable to WT (*SI Appendix*, Fig. S4). These results confirmed the two-site model of receptor–chemokine interaction, in which CRS1 is responsible for the initial recruitment of chemokines but does not alter the downstream G protein signaling, while CRS1.5 and CRS2 contribute more to the potency and efficacy of chemokine activation of G proteins.

Computational Analysis of KSHV-GPCR Activation Dynamics. To further examine molecular details in the dynamics of constitutive activation and CXCL1 chemokine activation of KSHV-GPCR, we performed all-atom molecular dynamics simulations. In the constitutively active structure, the interactions between $R^{6.62}$ and E^{ECL2} are observed, and polar contact pairs $Y^{3.37}$-$S^{5.42}$ and $R^{5.39}$-$D^{6.58}$ are also maintained throughout the simulation (*SI Appendix*, Fig. S5 *A* and *B*). In CXCL1-bound KSHV-GPCR structure, the distances between E6 of CXCL1-$R^{6.62}$, E^{ECL2}-$R^{6.62}$, $Y^{3.37}$-$S^{5.42}$, and $R^{5.39}$-$D^{6.58}$ are maintained throughout the 5 replicas of 1 μs simulation (*SI Appendix*, Fig. S5 *A* and *B*). These data demonstrate the thermostability of the constitutively active and CXCL1-bound KSHV-GPCR structures, providing computational support to the engagement of ECL2 in the constitutive activation of KSHV-GPCR.

Next, we analyzed the intramolecular interactions between CXCL1 and KSHV-GPCR. The surface electrostatic potential of the N terminus of KSHV-GPCR is negative, while the globular core of CXCL1 carries positive charges. The complementary charges between the chemokine and receptor facilitate CXCL1 recognition by KSHV-GPCR (*SI Appendix*, Fig. S5*C*). The orientation of CXCL1 in the transmembrane binding pocket is mainly supported by hydrogen bonds and salt bridges between the chemokine and the receptor (*SI Appendix*, Fig. S5 *D* and *F*). In CRS1, $T8^{NT}$ of KSHV-GPCR forms hydrogen bonds with N27 of CXCL1, $E15^{NT}$ interacts with K21 of CXCL1 via salt bridges and hydrogen bonds, $E19^{NT}$ interacts with K61 of CXCL1 through salt bridges and hydrogen bonds, and $S37^{NT}$ interacts with Q13 and C51 through multiple hydrogen bonds (*SI Appendix*, Fig. S5*D*). In CRS1.5, salt bridge dominates the interaction between sidechains of $E40^{NT}$ and K49, and multiple hydrogen bonds and water bridges support the hydrogen bond network between $R^{6.64}$, $R^{7.28}$, C9, and C11 (*SI Appendix*, Fig. S5*E*). The sidechain amine nitrogen of $R^{6.64}$ forms a hydrogen bond with the backbone carbonyl oxygen of C11, and the two sidechain amine nitrogen atoms of $R^{7.28}$ form hydrogen bonds with the backbone carbonyl oxygen of C11 and C9, respectively. In CRS2, extensive polar interactions secure the binding between the chemokine N terminus and the receptor transmembrane binding pocket (*SI Appendix*, Fig. S5*F*). R8 of CXCL1 uses one of its sidechain amine nitrogen atoms to form hydrogen bonds and salt bridges with the sidechain oxygen of $D^{6.58}$, and another amine nitrogen to form hydrogen bonds with the sidechain oxygen of $N^{7.32}$. Moreover, CXCL1 uses E6 to form extensive salt bridge network with the sidechains of $R^{5.39}$, $R^{5.35}$, and $R^{6.62}$. At the proximal N terminus of CXCL1, S2 and A1 are involved in a hydrogen bond network with water bridges, further enhancing the dynamic interactions between CXCL1 and KSHV-GPCR. The sidechain oxygen of S2 has multiple hydrogen bonds with the sidechain of $R^{4.64}$, and $E^{3.28}$, while A1 utilizes its backbone amine nitrogen to form hydrogen bonds with sidechain oxygen atoms of $E^{2.60}$ and $E^{3.28}$. The extensive salt bridge network formed between E6, R8, and the receptor binding pocket further strengthens CRS2 interactions between CXCL1 and KSHV-GPCR. Altogether, data from MD simulation support the cryo-EM structures of constitutively active and CXCL1-bound KSHV-GPCR and together provide molecular insights into the interaction dynamics between CXCL1 and KSHV-GPCR.

Comparison of Chemokine Binding Mode Between KSHV-GPCR and CXCR2. Given the structural homology and binding mode similarity between KSHV-GPCR and CXCR2, it is speculated that KSHV-GPCR is hijacked from CXCR2-expressing host cells by KSHV (6). We therefore further compared the structures of CXCL1-bound KSHV-GPCR and CXCL8-bound CXCR2 (*SI Appendix*, Fig. S6 *A* and *B*). Compared with CXCL8–CXCR2 interactions, the N terminus of CXCL1 protrudes 7.9 Å deeper into the KSHV-GPCR receptor binding cavity at CRS2 (*SI Appendix*, Fig. S6 *A*, *Left*), and the globular core of CXCL1 rotates ~40° counterclockwise from an extracellular point of view (*SI Appendix*, Fig. S6 *A*, *Right*). A series of counterclockwise inward bends are observed at the extracellular regions of TM1, 2, and 3. The top of TM loop 4 bends slightly outward, and TM7 displays an inward movement to the center of the chemokine binding pocket (*SI Appendix*, Fig. S6*B*).

Molecular Switches of KSHV-GPCR and Their Roles in Ligand-Independent Activation. To answer the question of how KSHV-GPCR has structurally evolved from its host analog into a constitutively active receptor, we examined the molecular switches conserved among class A GPCRs. The structure of KSHV-GPCR was aligned with that of CXCR2 in either active state (Fig. 4 *C–E* and *SI Appendix*, Fig. S6) or inactive state (Fig. 4 *A*, *B*, and *F–H*), and the structural motifs $N^{7.49}P^{7.50}xxY^{7.53}$, $CW^{6.48}xP^{6.50}$, $P^{5.50}$-$I^{3.40}$-$F^{6.44}$ were compared. In the NPxxY motif, $N^{7.49}$ is substituted by valine in KSHV-GPCR (expressed as $V/N^{7.49}$). In $CW^{6.48}xP^{6.50}$, the highly conserved $W^{6.48}$ is substituted by a cysteine ($C/W^{6.48}$) that greatly alters the spatial occupancy. Since substitution at these conserved motifs may create hyperactive or constitutively active class A GPCRs (26, 27), we further looked into the details of the geometry of residues lining these structural motifs (Fig. 4 *C–H*).

$N^{7.49}P^{7.50}xxY^{7.53}$ motif in class A GPCR mediates the transition from inactive to active conformation for G protein binding. However, the mutation of $V^{7.49}$ back to asparagine did not markedly change the constitutive activity of the receptor. Alanine substitution was conducted at $V^{7.49}$, $P^{7.50}$, and $Y^{7.53}$, respectively. No significant change in the extent of constitutive G protein dissociation was observed, suggesting that other players may also participate in the activation process.

Another structural motif, $CW^{6.48}xP^{6.50}$ is mutated to $CC^{6.48}xP^{6.50}$. This "toggle switch" motif works as a rotamer switch, bending the cytoplasmic half of TM6 outward to accommodate the binding of G protein. By converting to cysteine at this position, the residue with a smaller side chain can rearrange the orientation of TM6 for activation (Fig. 4 *D* and *G*). Indeed, by mutating $C^{6.48}$ back to tryptophan, the constitutive G protein activation was reduced significantly. This implies the importance of $C^{6.48}$ in constitutive G protein activation.

Next, we analyzed the $P^{5.50}$-$I^{3.40}$-$F^{6.44}$ motif, which forms an interface between TM3, TM5, and TM6. The conformational change of this motif is responsible for the outward displacement of TM6. The orientations of residue side chains in this motif are nearly identical to those in an active CXCR2, favoring G protein activation (Fig. 4 *E* and *H*). Alanine substitution at $P^{5.50}$ and $F^{6.44}$ abrogated the constitutive G protein dissociation, but alanine substitution of $I^{3.40}$ did not significantly affect the constitutive activation of KSHV-GPCR (see Fig. 4, *Table Inset*).

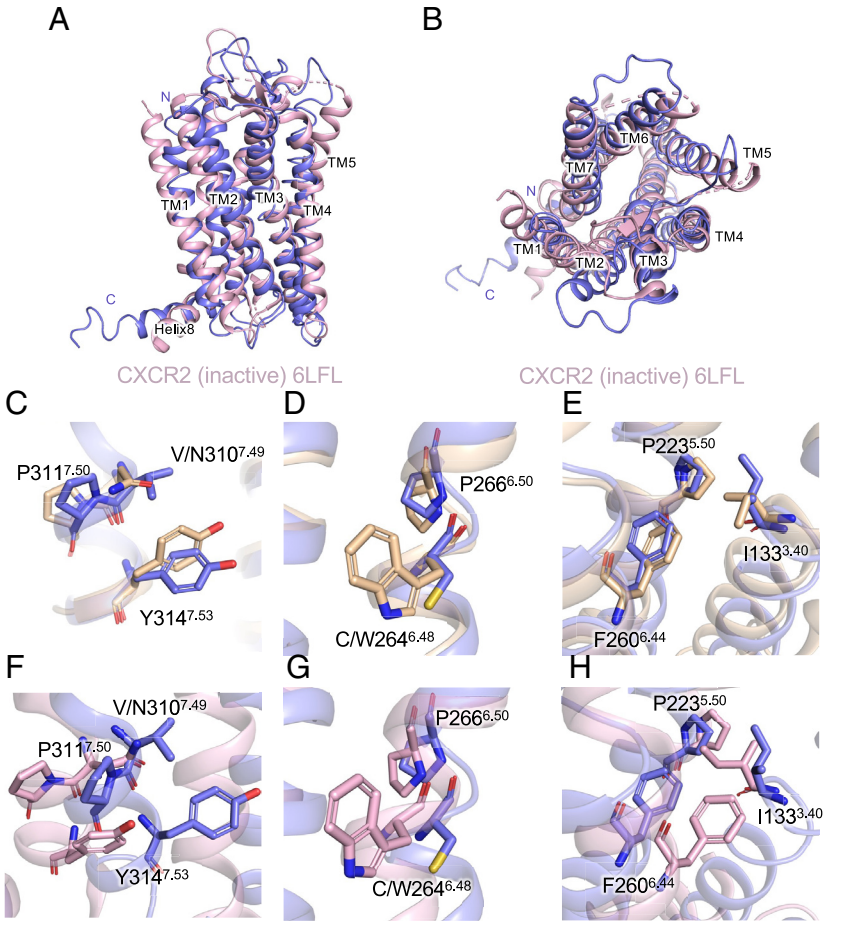

Variants	G protein dissociation response (% of WT)	*p* value	Expression (% of WT)
WT	100%	N/A	100%
I133A	110.5 ± 3.365	0.0179	97.49 ± 9.37
P223A	29.3 ± 2.683	<0.0001	94.55 ± 4.83
F260A	57.86 ± 8.234	<0.0001	81.98 ± 6.83
C264W	73.04 ± 2.814	<0.0001	130.0 ± 5.20
P266A	96.79 ± 5.657	0.336	90.94 ± 4.98
V310A	113.7 ± 3.304	0.0014	94.31 ± 1.33
V310N	106.2 ± 4.31	0.2515	101.6 ± 2.04
P311A	91.62 ± 1.103	0.0758	95.62 ± 2.44
Y314A	84.87 ± 3.754	0.0005	87.52 ± 0.18

Fig. 4. Comparison of conserved structural motifs between active KSHV-GPCR and either active or inactive CXCR2. (*A*) Side view of superimposed KSHV-GPCR (purple) and inactive CXCR2 (light pink). (*B*) Top view of superimposed KSHV-GPCR (purple) and inactive CXCR2 (light pink). (*C–E*) Detailed comparison between KSHV-GPCR (purple) and active CXCR2 (wheat gold). (*C*) NPxxY motif, (*D*) $P^{6.50}$-C/$W^{6.48}$ "toggle switch", and (*E*) $P^{5.50}$-$I^{3.40}$-$F^{6.44}$ motif were compared. (*F–H*) Detailed comparison between KSHV-GPCR (purple) and inactive CXCR2 (light pink). (*F*) NPxxY motif, (*G*) $P^{6.50}$-C/$W^{6.48}$ "toggle switch", and (*H*) $P^{5.50}$-$I^{3.40}$-$F^{6.44}$ motif were compared. (*Table*) Basel levels of NanoBiT signals in G protein dissociation assay. Residues of these structural motifs were substituted by alanine. Readouts were normalized and shown as percentages of G protein response of WT strain.

Altogether, based on structural geometry and signaling properties at these conserved molecular switch motifs, our KSHV-GPCR structural model supports an active conformation. Among these highly conserved residues, some substitutions found exclusively at KSHV-GPCR may contribute to its constitutive activation by reshaping the G protein binding cavity.

Receptor–Gi Interface of KSHV-GPCR Compared with Active and Inactive CXCR2. Next, we examined the receptor–Gi interface of KSHV-GPCR. The DRY motif forms direct polar contact with the Gαi protein and is crucial for G protein activation. In KSHV-GPCR, $D^{3.49}$ is substituted by valine. By reversely mutating valine at position 3.49 back to D, no significant deviation in the extent of G protein activation was observed. Polar interactions between the receptor and Gαi protein involve $R^{3.50}$-C351, $L^{3.53}$-N347, as well as $Q^{6.28}$-E318 pairs (Fig. 5). Alanine substitution of $R^{3.50}$ and $L^{3.53}$ resulted in a loss of G protein activity, while for the $Q^{6.28}$A mutant, no significant difference was observed. The ionic interactions in the G protein binding cavity are highly important for G protein activation. Despite the high overall similarity in structures between KSHV-GPCR and the active CXCR2, there are some differences at the receptor–Gi interfaces (Fig. 5 *A* and *B*). First, a displacement toward the cytoplasm is observed for TM3, resulting in a deeper protrusion of the α5 helix of the Gαi protein into the G protein binding cavity. Secondly, the intracellular loop 2 (ICL2) of KSHV-GPCR is closer to the Gi

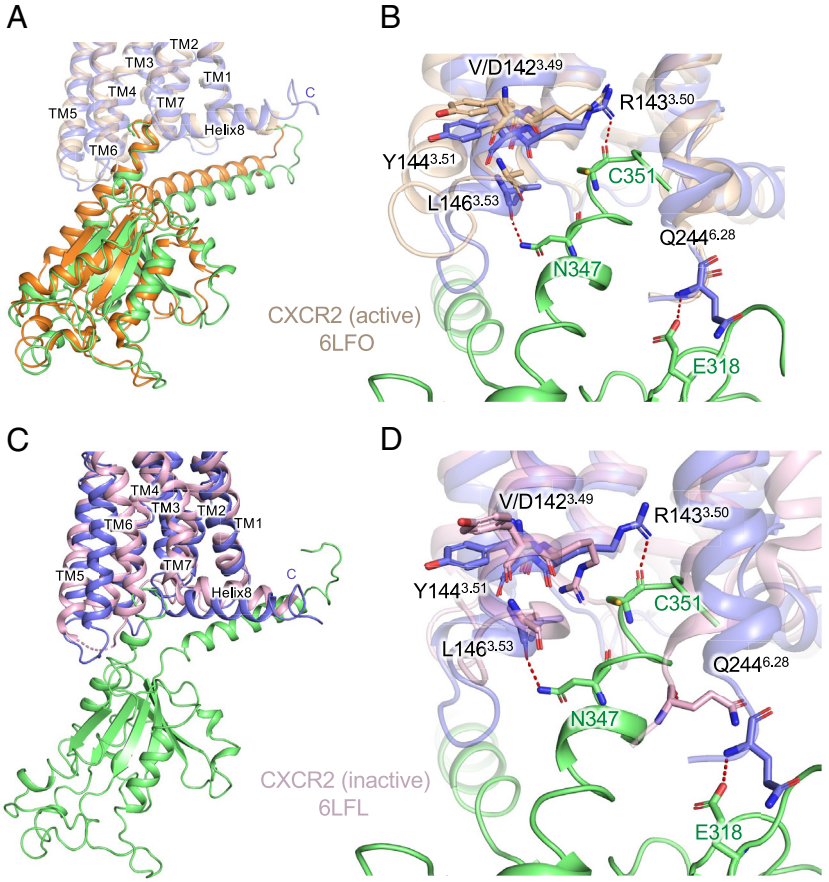

Mutants	G protein dissociation response (% of WT)	*p* value	Expression (% of WT)
WT	100%	N/A	100%
V142A	85.57 ± 2.396	0.0014	109.9 ± 17.08
V142D	105 ± 4.476	0.7027	111.9 ± 17.70
R143A	36.11 ± 3.191	<0.0001	82.05 ± 0.62
L146A	37.69 ± 1.867	<0.0001	116.1 ± 7.102
Q244A	93.91 ± 2.588	0.471	122.2 ± 14.12

Fig. 5. Comparison of receptor–Gαi interface between active KSHV-GPCR and either active or inactive CXCR2. (*A*) Side view of superimposed KSHV-GPCR (purple) and active CXCR2 (wheat gold) in complex with Gαi protein (green). (*B*) Close-up view of superimposed KSHV-GPCR (purple) and active CXCR2 (wheat gold) in complex with Gαi protein (green). Residues with polar interaction were highlighted in sticks. (*C*) Side view of superimposed KSHV-GPCR (purple) and inactive CXCR2 (light pink) in complex with Gαi protein (green). (*D*) Close-up view of superimposed KSHV-GPCR (purple) and inactive CXCR2 (light pink) in complex with Gαi protein (green). (*Table*) Basel levels of NanoBiT signals in G protein dissociation assay. Alanine substitution was conducted to residues at receptor–Gi interface of KSHV-GPCR. Readouts were normalized and shown as percentages of G protein response of the WT.

protein, while in active CXCR2, ICL2 bends outward. By comparing the inactive CXCR2 structure with the KSHV-GPCR structure, several distinct features support the active state model of KSHV-GPCR (Fig. 5 *C* and *D*). In TM3, the geometry and position of the DRY motif are similar in both structures, yet $R^{3.50}$ in KSHV-GPCR takes a more relaxed pose, with better contact to the α5 helix in the G protein binding cavity. The outward movement of TM6 of KSHV-GPCR in its active state allows direct contact between $Q^{6.28}$ and Gαi protein, while the ICL3 and adjacent TM6 in the inactive CXCR2 structure is distant from the active conformation. These results indicate that the G protein-activating capacity of KSHV-GPCR is robust, given the orientations and geometry of its TM3 residues lining the G protein binding cavity.

Discussion

In this work, we present cryo-EM structures of KSHV-GPCR in active conformation. KSHV-GPCR, encoded by ORF74, is up-regulated in the lytic cycle of HHV-8 and is responsible for angiogenesis and oncogenic transformation of Kaposi's sarcoma (8). Exogenous expression of KSHV-GPCR in mice led to Kaposi's sarcoma-like pathological changes (11), indicating a crucial function of the constitutively active receptor in oncogenic transformation. Based on our cryo-EM model of the unliganded KSHV-GPCR, ECL2 is essential for the constitutive activity. ECL2 folds back to the opening of the TM pocket and forms polar interaction with KSHV-GPCR through the $E198^{ECL2}$-$R278^{6.62}$ pair. Disruption of this polar interaction with alanine substitution of $R278^{6.62}$ reduced the constitutive activity, as was measured by cAMP response and NanoBiT-based G protein dissociation assays. Moreover, the substitution of ECL2 with its counterparts of CXCR2, FPR1, CXCR4, and CMKLR1, all depending on agonist binding for receptor activation, abrogated constitutive activation of the resulting chimeras. At the receptor–Gi protein interface, there is no significant change between the unliganded and CXCL1-bound KSHV-GPCR, suggesting that ECL2 is able to hold the receptor in an active conformation for Gi protein activation. It is worth noting that, the assays used for measuring constitutive activity of KSHV-GPCR may not quantitatively reflect the absolute extent of receptor basal activities, as the assay readouts may be affected by protein expression levels. Despite the mutants and chimeric receptors

used in this study having comparable cell surface expression as measured by flow cytometry, the assay readouts only provide a relative comparison of constitutive activities among the mutated receptors. Therefore, caution should be taken when interpreting these results.

Constitutive activity was also observed in other viral GPCRs, notably US28 from human cytomegalovirus (HCMV) and BILF1 from Epstein–Barr virus (EBV). US28 has a TM pocket for binding of CX3CL1 in a different mode (6). Nevertheless, the two-site model applies to these interactions between the receptor and its various ligands. US28 displays constitutive activity through Gi, Gq, and G12/13 pathways. However, the binding of CX3CL1 to US28 is context-dependent, as this ligand can serve as either a partial agonist or an inverse agonist (28). In contrast, BILF1 does not have an identified chemokine ligand, and its TM pocket is occluded by the ECL2 (18). This structural feature is responsible for the EBV oncogenic function of BILF1 by inducing constitutive signaling mainly through the Gi proteins (18). Like BILF1, KSHV-GPCR has an occluded orifice due to polar interactions between ECL2 and the side chain of TM3, TM5, and TM6. However, KSHV-GPCR differs from other viral GPCRs in that it binds a number of CC and CXC chemokines that further activate the receptor. Based on sequence comparison, KSHV-GPCR has the highest homology with human CXCR2 (27% identical amino acids). Therefore, KSHV-GPCR is likely a CXCR hijacked by the virus. In this study, we chose CXCL1, also termed GROα for its melanoma growth-stimulating activity and transforming capability through CXCR2. Our structural model shows a clearly defined TM pocket that accommodates CXCL1 and serves as CRS2. CXCL1 binding disrupts the polar interactions between ECL2 and the side chain of TM3, TM5, and TM6 but maintains the active conformation of KSHV-GPCR based on structural comparison of the unliganded and CXCL1-bound receptor. At CRS2, the ELR motif of CXCL1 is a critical determinant of the potency of the agonist by polar interactions between E6 and $R212^{5.39}$. In addition, R8 interacts with both $D274^{6.58}$ and $N293^{7.32}$. Disruption of these important interactions at CRS2 abrogates the CXCL1-induced G protein dissociation, confirming that CRS2 is essential to the induced activation of KSHV-GPCR by the chemokine.

Before high-resolution chemokine receptor structures became available, domain-swapping experiments were carried out and led to the prediction that the N terminus of KSHV-GPCR is necessary for the binding of chemokine ligands but not for transmembrane signaling (29). The N terminus of KSHV-GPCR (a.a. 1 to 47) contains a stretch of negatively charged amino acids, notably 12-DDDE-15. Moreover, the disulfide bond between the PC motif (VC in KSHV-GPCR) and $C286^{ECL3}$ is not found in this structure. These features presumably make the N terminus of the receptor more flexible in the initial interaction with chemokines at CRS1. In the reconstructed 3D model of CXCL1-bound KSHV-GPCR–Gi complex, the receptor N terminus wraps around the globular core of CXCL1. Analysis of a fully settled CXCL1 in the TM pocket shows $D13^{NT}$ interaction with K21 of CXCL1 and $Y26^{NT}$ interaction with K61. These polar interactions serve to stabilize the bound chemokine. As a transition from CRS1 to CRS2, CRS1.5 contains several residues in the receptor N terminus that interact with the N-loop and β3-strand of CXCL1, including Q10, L12, Q13 of the N-loop and K49 of the β3-strand. These interactions may be helpful in guiding the N terminus of the chemokine into the TM pocket, as indicated by data from our mutagenesis assay.

Early studies, conducted shortly after the discovery of KSHV-GPCR, focused on key residues that profoundly influence the constitutive activity of the receptor (30). These studies did not identify key residues unique to KSHV-GPCR. For example, the substitution of $R143^{3.50}$, which is a part of the critical DRY motif, abolished all Class A GPCR signaling. This and other findings suggest that the constitutive activity of KSHV-GPCR is the combined outcome of mutations of the hijacked receptor gene in the virus (26, 30). Nevertheless, the "ionic lock" characterized by the interaction between $D/E^{3.49}$, $R^{3.50}$, and $D/E^{6.30}$ stabilizes the inactive conformation of GPCRs (31). In KSHV-GPCR, $D/E^{3.49}$ and $D/E^{6.30}$ are substituted by $V^{3.49}$ and $R^{6.30}$, respectively. As demonstrated by previous studies and in line with our mutagenesis data, $V^{3.49}D$ substitution did not decrease the constitutive activity of the receptor. Besides, the geometry of $R^{6.30}$ is distant from $V^{3.49}$ and $R^{3.50}$, thereby disrupting the "ionic lock". Another important and conserved residue, $W^{6.48}$ for TM6 conformational change, is substituted by cysteine in KSHV-GPCR. This mutation may have a strong impact on KSHV-GPCR constitutive activity, as $C^{6.48}W$ disrupted the ligand-independent G protein activation. The canonical NPxxY motif is characterized by a hydrogen bond network between $N^{7.49}$ and $D^{2.50}$. However, these residues are mutated to $V^{7.49}$ and $S^{2.50}$ in KSHV-GPCR, respectively. The two residues are distant from each other, which is unable to support the canonical hydrogen bond network. As evidenced in our study and other biochemical studies, $V^{7.49}N$ and $S^{2.50}D$ mutations did not alter the constitutive activity. Previous studies suggested the importance of $L^{2.48}$ and $L^{2.51}$ in constitutive activity, as the $L^{2.48}D$ and $L^{2.51}D$ mutants diminished the constitutive activity but could still be activated by chemokine ligands, and KS lesions were absent in transgenic mice carrying $L^{2.48}D$ mutant (11, 32). In line with their hypothesis, $L^{2.48}$ and $L^{2.51}$ in our KSHV-GPCR structures indeed face the lipid bilayer, supporting the active conformation in both unliganded and CXCL1-bound KSHV-GPCR. Substitution by charged amino acids may destabilize the active conformation of the receptor, thus requiring extra energy (ligand binding) for effective conformational changes toward activation.

In conclusion, our cryo-EM model provides the structure of a CXC chemokine bound to a viral GPCR that possesses both constitutive and ligand-induced activities. Moreover, this study also provides the first high-resolution structure of CXCL1 bound to a chemokine receptor. These pieces of structural information will likely shed light on how viral GPCRs maintain constitutive activity, which may help us to understand chemokine binding and activation mechanisms in general.

Materials and Methods

Generation of Recombinant CXCL1. The coding sequence of human CXCL1 with a C-terminal His6-tag was modified with a glycoprotein 67 (gp67) signal peptide. The construct was expressed in *Sf*9 insect cells as secreted proteins using the baculovirus infection system. The media were collected after infection for 48 h and subjected to affinity chromatography purification. For details, please refer to *SI Appendix, Materials and Methods*.

Preparation of apo-KSHV-GPCR–Gi and CXCL1-KSHV-GPCR–Gi Complexes. The full-length KSHV-GPCR was used to obtain apo and CXCL1-bound signaling complexes. The N termini of the KSHV-GPCR coding sequence were modified with a hemagglutinin peptide sequence, followed by a FLAG-tag, a human rhinovirus 3C (HRV 3C) protease cleavage site, and a thermostabilized apocytochrome b562RIL (BRIL) as a fusion protein to increase protein expression and stability. A dominant-negative Gαi1 (DNGαi1) was cloned into a pFastbac1 vector and Gβ1γ2 was cloned into a pFastBac-Dual vector, respectively.

For expression of apo-KSHV-GPCR–Gi complex, the KSHV-GPCR, DNGαi1, Gβ1γ2 were coexpressed in Sf9 insect cells at a viral infection ratio of 1:1:1 when the cell density reached 2 × 10^6 cells per ml. After 48 h of infection, the cells were collected for further purification. For expression of CXCL1–KSHV-GPCR–Gi complex, the baculovirus of CXCL1 was also added as the same ratio as KSHV-GPCR to facilitate the signaling complex formation.

For the purification of the apo-KSHV-GPCR–Gi complex, cell pellets from 2 L of culture were thawed at room temperature and suspended in the lysis buffer, lysed, and the complex was extracted from the membrane fraction for affinity chromatography purification. For the CXCL1-KSHV-GPCR–Gi complex, the same steps were performed by adding purified CXCL1 during the process of protein purification. These experiments are described in detail in *SI Appendix, Materials and Methods*.

Cryo-EM Grid Preparation and Data Collection. For the cryo-EM grid preparation of the purified complexes, the proteins were deposited onto glow-discharged holey grids (Quantifoil). Then, the grids were blotted and vitrified by plunging into liquid ethane in a Vitrobot Mark IV (Thermo Fisher Scientific). Cryo-EM images were obtained by a Titan Krios C3i cryo-TEM (Thermo Fisher Scientific) operating at 300 kV, using a K3 Summit detector (Gatan, Pleasanton, CA) with a pixel size of 0.85 Å. The procedures are detailed in *SI Appendix, Materials and Methods*.

Data Processing and Three-Dimensional Reconstruction. The software cryoSPARC version v4.2.1 (Structura Biotechnology, Toronto, Canada) was used to perform single particle analysis of the complexes. Multiple rounds of refinements generated an EM map [Coulomb potential map (33)] of apo-KSHV-GPCR–Gi with an estimated global resolution of 2.81 Å at a Fourier shell correlation of 0.143. And for the CXCL1–KSHV-GPCR–Gi complex, the EM density map yielded an indicated global resolution of 3.01 Å at a Fourier shell correlation of 0.143. Details are included in *SI Appendix, Materials and Methods*.

Model Building, Structure Refinement, and Figure Preparation. The models were manually built in COOT-0.9.8. Real-space refinements were performed using Phenix. The model statistics were validated using MolProbity. Structural figures were prepared in Chimera and PyMOL (https://pymol.org/2/). The final refinement statistics are provided in *SI Appendix*, Table S1. The maximum distance cut-off for polar hydrogen bond interactions and hydrophobic interactions were set at 3.5 Å and 4.5 Å, respectively.

MD Simulations. System preparation and Molecular Dynamics (MD) simulations were performed following the detailed protocol in (34). Details are described in *SI Appendix, Materials and Methods*.

The analysis of the resulting trajectories was performed using MDAnalysis (35), visualization and image rendering were performed with PyMOL, and graphical representations were obtained with the Seaborn Package (36).

Mutagenesis Study. Wild-type and mutant KSHV-GPCR were cloned into the pcDNA3.1(+) vector (Invitrogen). The coding sequences were chemically synthesized (General Biol.) and mutagenized by overlap PCR using the ClonExpress Ultra One Step Cloning Kit (Vazyme Biotech; C115). All constructs were verified by DNA sequencing (Genewiz).

cAMP Inhibition Assay. HeLa cells were transfected with receptor plasmids using Lipofectamine 3000 (Invitrogen) for 24 hrs. For the constitutively active KSHV-GPCR model, different plasmid DNA concentrations were applied for transfection. Cells were harvested and subjected to cAMP detection using the LANCE Ultra cAMP kit (#TRF0263; PerkinElmer Life Sciences, Waltham, MA) following the manufacturer's instructions. Signals for cAMP levels were collected using an Envision 2105 multimode plate reader (PerkinElmer).

NanoBiT-Based G Protein Dissociation Assay. HEK293T cells were seeded and cotransfected with pcDNA3.1(+) vector encoding KSHV-GPCR (WT/mutants), pcDNA3.1-Gαi1-LgBiT, pcDNA3.1-Gβ1, and pcDNA3.1-SmBiT-Gγ2. After 24 hrs transient expression, cells were collected and loaded onto a 384-well white plate and incubated with 10 μM coelenterazine H for 2 hrs at room temperature (Yeasen Biotech, Shanghai, China). Luminescence signals were read by an Envision 2105 multimode plate reader (PerkinElmer). This experiment is described in detail in *SI Appendix*, Materials and Methods.

Surface Expression Analysis. Cells were transfected with FLAG-tagged WT or mutant KSHV-GPCR expression vectors for 24 hrs at 37 °C. Then, cells were harvested and stained with an Alexa Fluor™ 488-labeled anti-FLAG antibody (L5; Invitrogen, Cat # MA1-142; 1:50 diluted by HBSS buffer) for 60 mins on ice. The fluorescence signals for the antibody–receptor complex on the cell surface were then quantified by flow cytometry (CytoFLEX, Beckman Coulter, Brea, CA). The experiment procedure is detailed in *SI Appendix*, Materials and Methods.

Statistical Analysis. For all cellular assays, at least three independent experiments were performed in duplicates. The data were expressed as mean ± standard error of means (SEM), and data analysis was performed in GraphPad Prism version 9.5.0. Analysis of Variance (ANOVA) using the one-way method was applied for statistical comparison. A *P*-value of 0.05 or lower is considered statistically significant.

Data, Materials, and Software Availability. Cryo-EM density maps of KSHV-GPCR-Gi complex and CXCL1-KSHV-GPCR-Gi complex resolved in this study and the associated atomic coordinates have been deposited in the Electron Microscopy Data Bank (EMDB entry ID: EMD-36889; EMD-36888) and in the Protein Data Bank (PDB entry ID: 8K4P, 8K4O), respectively (37–40). All other data are included in the manuscript and/or *SI Appendix*.

ACKNOWLEDGMENTS. This work was supported by National Natural Science Foundation of China 82402140 (A.L.), Shenzhen Science and Technology Program Grant No. RCBS20221008093330067 (A.L.), and National Natural Science Foundation of China 32070950 (R.D.Y.). This work was also supported in part by Grants from the Science, Technology and Innovation Commission of Shenzhen Municipality GXWD20201231105722002-20200831175432002 (R.D.Y.), China Postdoctoral Science Foundation 2022M713049 (A.L.), Starts-up funds from the Dongguan Songshan Lake Central Hospital (A.L.), the Ganghong Young Scholar Development Fund (R.D.Y.), the fund from Kobilka Institute of Innovative Drug Discovery at The Chinese University of Hong Kong, Shenzhen (R.D.Y.), and the fund from Shenzhen-Hong Kong Cooperation Zone for Technology and Innovation (HZQB-KCZYB-2020056).

Author affiliations: [a]Kobilka Institute of Innovative Drug Discovery, School of Medicine, The Chinese University of Hong Kong, Shenzhen, Guangdong 518172, China; [b]Dongguan Songshan Lake Central Hospital, Dongguan Third People's Hospital, The Affiliated Dongguan Songshan Lake Central Hospital, Guangdong Medical University, Dongguan, Guangdong 523326, China; [c]Laboratori de Medicina Computacional, Unitat de Bioestadística, Facultat de Medicina, Universitat Autònoma de Barcelona, Bellaterra 08193, Spain; and [d]The Chinese University of Hong Kong, Shenzhen Futian Biomedical Innovation Research and Development Center, Shenzhen, Guangdong 518048, China

1. M. Karamanou, C. Antoniou, A. J. Stratigos, Z. Saridaki, G. Androutsos, The eminent dermatologist Moriz Kaposi (1837–1902) and the first description of idiopathic multiple pigmented sarcoma of the skin. *J. BUON* **18**, 1101–1105 (2013).
2. E. A. Mesri, E. Cesarman, C. Boshoff, Kaposi's sarcoma and its associated herpesvirus. *Nat. Rev. Cancer* **10**, 707–719 (2010).
3. P. H. Goncalves, J. Ziegelbauer, T. S. Uldrick, R. Yarchoan, Kaposi sarcoma herpesvirus-associated cancers and related diseases. *Curr. Opin. HIV AIDS* **12**, 47–56 (2017).
4. P. S. Moore, C. Boshoff, R. A. Weiss, Y. Chang, Molecular mimicry of human cytokine and cytokine response pathway genes by KSHV. *Science* **274**, 1739–1744 (1996).
5. T. W. M. De Groof *et al.*, Viral G protein-coupled receptors: Attractive targets for herpesvirus-associated diseases. *Pharmacol. Rev.* **73**, 828–846 (2021).
6. M. M. Rosenkilde, N. Tsutsumi, J. M. Knerr, D. F. Kildedal, K. C. Garcia, Viral G protein-coupled receptors encoded by beta- and gamma-herpesviruses. *Annu. Rev. Virol.* **9**, 329–351 (2022).
7. L. Arvanitakis, E. Geras-Raaka, A. Varma, M. C. Gershengorn, E. Cesarman, Human herpesvirus KSHV encodes a constitutively active G-protein-coupled receptor linked to cell proliferation. *Nature* **385**, 347–350 (1997).
8. C. Bais *et al.*, G-protein-coupled receptor of Kaposi's sarcoma-associated herpesvirus is a viral oncogene and angiogenesis activator. *Nature* **391**, 86–89 (1998).
9. A. G. Polson, D. Wang, J. DeRisi, D. Ganem, Modulation of host gene expression by the constitutively active G protein-coupled receptor of Kaposi's sarcoma-associated herpesvirus. *Cancer Res.* **62**, 4525–4530 (2002).
10. R. Masood *et al.*, Vascular endothelial growth factor/vascular permeability factor is an autocrine growth factor for AIDS-Kaposi sarcoma. *Proc. Natl. Acad. Sci. U.S.A.* **94**, 979–984 (1997).
11. E. Cesarman, E. A. Mesri, M. C. Gershengorn, Viral G protein-coupled receptor and Kaposi's sarcoma: a model of paracrine neoplasia? *J. Exp. Med.* **191**, 417–422 (2000).

12. M. Schwarz, P. M. Murphy, Kaposi's sarcoma-associated herpesvirus G protein-coupled receptor constitutively activates NF-kappa B and induces proinflammatory cytokine and chemokine production via a C-terminal signaling determinant. *J. Immunol.* **167**, 505–513 (2001).
13. L. W. Shepard *et al.*, Constitutive activation of NF-kappa B and secretion of interleukin-8 induced by the G protein-coupled receptor of Kaposi's sarcoma-associated herpesvirus involve G alpha(13) and RhoA. *J. Biol. Chem.* **276**, 45979–45987 (2001).
14. H. G. Guo *et al.*, Kaposi's sarcoma–like tumors in a human herpesvirus 8 ORF74 transgenic mouse. *J. Virol.* **77**, 2631–2639 (2003).
15. L. Coscoy, Immune evasion by Kaposi's sarcoma-associated herpesvirus. *Nat. Rev. Immunol.* **7**, 391–401 (2007).
16. C. Areste, D. J. Blackbourn, Modulation of the immune system by Kaposi's sarcoma-associated herpesvirus. *Trends Microbiol.* **17**, 119–129 (2009).
17. J. P. Couty, E. Geras-Raaka, B. B. Weksler, M. C. Gershengorn, Kaposi's sarcoma-associated herpesvirus G protein-coupled receptor signals through multiple pathways in endothelial cells. *J. Biol. Chem.* **276**, 33805–33811 (2001).
18. N. Tsutsumi *et al.*, Structural basis for the constitutive activity and immunomodulatory properties of the Epstein–Barr virus-encoded G protein-coupled receptor BILF1. *Immunity* **54**, 1405–1416.e7 (2021).
19. N. Tsutsumi *et al.*, Atypical structural snapshots of human cytomegalovirus GPCR interactions with host G proteins. *Sci. Adv.* **8**, eabl5442 (2022).
20. M. C. Gershengorn, E. Geras-Raaka, A. Varma, I. Clark-Lewis, Chemokines activate Kaposi's sarcoma-associated herpesvirus G protein-coupled receptor in mammalian cells in culture. *J. Clin. Invest.* **102**, 1469–1472 (1998).
21. J. A. Ballesteros, H. Weinstein, "Integrated methods for the construction of three-dimensional models and computational probing of structure-function relations in G protein-coupled receptors" in *Methods in Neurosciences*, S. C. Sealfon, Ed. (Academic Press, 1995), **vol. 25**, pp. 366–428.
22. W. I. Weis, B. K. Kobilka, The molecular basis of G protein-coupled receptor activation. *Annu. Rev. Biochem.* **87**, 897–919 (2018).
23. A. S. Dixon *et al.*, Nanoluc complementation reporter optimized for accurate measurement of protein interactions in cells. *ACS Chem. Biol.* **11**, 400–408 (2016).
24. D. J. Scholten *et al.*, Pharmacological modulation of chemokine receptor function. *Br. J. Pharmacol.* **165**, 1617–1643 (2012).
25. L. Urvas, E. Kellenberger, Structural insights into molecular recognition and receptor activation in chemokine-chemokine receptor complexes. *J. Med. Chem.* **66**, 7070–7085 (2023).
26. M. Burger *et al.*, Point mutation causing constitutive signaling of CXCR2 leads to transforming activity similar to Kaposi's sarcoma herpesvirus-G protein-coupled receptor. *J. Immunol.* **163**, 2017–2022 (1999).
27. O. Fritze *et al.*, Role of the conserved NPxxY(x)5,6F motif in the rhodopsin ground state and during activation. *Proc. Natl. Acad. Sci. U.S.A.* **100**, 2290–2295 (2003).
28. J. S. Burg *et al.*, Structural biology. Structural basis for chemokine recognition and activation of a viral G protein-coupled receptor. *Science* **347**, 1113–1117 (2015).
29. H. H. Ho, D. Du, M. C. Gershengorn, The N terminus of Kaposi's sarcoma-associated herpesvirus G protein-coupled receptor is necessary for high affinity chemokine binding but not for constitutive activity. *J. Biol. Chem.* **274**, 31327–31332 (1999).
30. H. H. Ho, N. Ganeshalingam, A. Rosenhouse-Dantsker, R. Osman, M. C. Gershengorn, Charged residues at the intracellular boundary of transmembrane helices 2 and 3 independently affect constitutive activity of Kaposi's sarcoma-associated herpesvirus G protein-coupled receptor. *J. Biol. Chem.* **276**, 1376–1382 (2001).
31. J. A. Ballesteros *et al.*, Activation of the beta 2-adrenergic receptor involves disruption of an ionic lock between the cytoplasmic ends of transmembrane segments 3 and 6. *J. Biol. Chem.* **276**, 29171–29177 (2001).
32. P. J. Holst *et al.*, Tumorigenesis induced by the HHV8-encoded chemokine receptor requires ligand modulation of high constitutive activity. *J. Clin. Invest.* **108**, 1789–1796 (2001).
33. J. Wang, P. B. Moore, On the interpretation of electron microscopic maps of biological macromolecules. *Protein Sci.* **26**, 122–129 (2017).
34. C. Llinas Del Torrent *et al.*, The Leu/Val(6.51) side chain of cannabinoid receptors regulates the binding mode of the alkyl chain of Delta(9)-tetrahydrocannabinol. *J. Chem. Inf. Model* **63**, 5927–5935 (2023).
35. N. Michaud-Agrawal, E. J. Denning, T. B. Woolf, O. Beckstein, MDAnalysis: A toolkit for the analysis of molecular dynamics simulations. *J. Comput. Chem.* **32**, 2319–2327 (2011).
36. M. L. Waskom, Seaborn: Statistical data visualization. *J. Open Source Softw.* **6**, 3021 (2021).
37. A. J. Liu, Y. Z. Liu, Cryo-EM structure of an active Kaposi's Sarcoma-Associated Herpesvirus-G Protein-Coupled Receptor (KSHV-GPCR) in complex with Gi protein. Protein Data Bank. https://www.rcsb.org/structure/8K4P. Deposited 20 July 2023.
38. A. J. Liu, Y. Z. Liu, Cryo-EM structure of Kaposi's Sarcoma-Associated Herpesvirus-G Protein-Coupled Receptor (KSHV-GPCR)in complex with CXC chemokine CXCL1. Protein Data Bank. https://www.rcsb.org/structure/8K4O. Deposited 20 July 2023.
39. A. J. Liu, Y. Z. Liu, Cryo-EM structure of an active Kaposi's Sarcoma-Associated Herpesvirus-G Protein-Coupled Receptor (KSHV-GPCR) in complex with Gi protein. Electron Microscopy Data Bank. https://www.ebi.ac.uk/emdb/EMD-36889. Deposited 20 July 2023.
40. A. J. Liu, Y. Z. Liu, Cryo-EM structure of Kaposi's Sarcoma-Associated Herpesvirus-G Protein-Coupled Receptor (KSHV-GPCR)in complex with CXC chemokine CXCL1. Electron Microscopy Data Bank. https://www.ebi.ac.uk/emdb/EMD-36888. Deposited 20 July 2023.